



Article

Structural Flexibility Effect on Spaceborne Solar Observation System's Micro-Vibration Response

Lin Yang^{1,2} , Yansong Wang^{1,2,*} , Lei Wei^{1,2} and Yao Chen^{1,2}

¹ Institute of Frontiers and Interdisciplinary Sciences, Shandong University, Binhai Road 72, Qingdao 266237, China; yanglincas@sdu.edu.cn (L.Y.); weilei0906@sdu.edu.cn (L.W.); yaochen@sdu.edu.cn (Y.C.)

² Institute of Space Sciences, Shandong University, Wenhua West Road 180, Weihai 264209, China

* Correspondence: wangyansong@sdu.edu.cn

Abstract: The spaceborne solar observation system is crucial for the study of space phenomena such as solar flares, which requires high tracking accuracy. This study presents a coupling model that integrates mechanical, electrical, and control models to investigate the structural flexibility effect on the micro-vibration response. We established a rigid–flexible model using mechanical parts. We considered the influence of flexible features while studying the dynamic responses in its operation. The state-space equations of the system showed that modal frequency, damping, and modal participation factors played significant roles. We derived transfer functions using the Laplace transform of the coupling models to better understand this mechanism, and Simulink models were thereby established. We simulated the acceleration responses of the rigid–flexible and rigid models under angle tracking modes, and the results showed significant differences. We also simulated the acceleration responses of the models under various control frequencies, and the optimal control frequency was thus obtained. Finally, we performed experiments, and the results indicated that the rigid–flexible model could better predict the motion and acceleration responses for the spaceborne solar observation system. This study provides valuable information for understanding the role of flexible features in space performance high-tracking accuracy instruments and for micro-vibration suppression research.

Keywords: satellites; 2D turntable; structural flexibility; micro-vibration; mechanical–electrical–control coupling; Simulink model



Citation: Yang, L.; Wang, Y.; Wei, L.; Chen, Y. Structural Flexibility Effect on Spaceborne Solar Observation System's Micro-Vibration Response. *Aerospace* **2024**, *11*, 65. <https://doi.org/10.3390/aerospace11010065>

Academic Editor: Hyun-Ung Oh

Received: 2 December 2023

Revised: 6 January 2024

Accepted: 8 January 2024

Published: 10 January 2024



Copyright: © 2024 by the authors. Licensee MDPI, Basel, Switzerland. This article is an open access article distributed under the terms and conditions of the Creative Commons Attribution (CC BY) license (<https://creativecommons.org/licenses/by/4.0/>).

1. Introduction

The Earth is influenced by powerful electromagnetic radiation and high-energy particle radiation released from solar activity. Solar flares are among the most violent explosions in the solar atmosphere and are a major focus of space science research [1,2]. Unfortunately, high-energy particles and electromagnetic solid radiation pose a fatal threat to space facilities and deep space exploration safety. High-energy particles can easily break through the surfaces of satellites, causing charging and discharging in satellites and even destroying spaceborne equipment [3]. A spaceborne solar observation system (SSOS) is an important tool for achieving the real-time tracking, observation, and analysis of the Sun. The SSOS must have high tracking accuracy to achieve real-time and accurate observation data.

The SSOS two-dimensional (2D) turntable presented in this study is a typical mechanical–electrical–control coupled system that generates disturbing forces and torques during the tracking rotation. These forces and torques are caused by manufacturing, assembly and control errors, posing a significant threat to spacecraft pointing and tracking stability, commonly known as the micro-vibration effect [4–7]. When these forces are coupled with structural modes, resonance will occur, which may cause catastrophic impacts in many fields, such as earthquakes [8,9]. In aerospace, resonance may cause a decrease in satellite pointing accuracy and stability accuracy, further affecting the performance of satellite

payloads [10]. Therefore, the flexible vibrations of the structure's turntable cannot be ignored and must be considered when designing SSOS systems.

When studying the published literature on the modeling of spaceborne 2D turntables, we discovered that the published literature is primarily focused on control system design [11,12], structural design, and structural dynamic modeling [13–17]. Wang [11] used non-magnetic technology to study turntable pointing accuracy and motion control, analyzed the influence of the servo control parameters on the dynamic performance and steady-state error, and tested the turntable angular positioning accuracy. Zou [15] investigated the micro-vibration characteristics of a spaceborne 2D turntable and conducted a modal and frequency response analysis of the structure, which were later verified by experiments. Yao [18] established the governing equations of the semi-rigid joints and integrated them into the dynamic equation of the deployable structure. The research mentioned above did not combine a control system model with a structural dynamics model. Moreover, the rigid–flexible coupling effect has not been considered, and the influence of structural high-frequency vibrations on the rigid body motion has been ignored. The challenge is that satellites and their payloads are extremely sensitive to high-frequency micro-vibrations, which can be particularly problematic for deep space exploration. For example, the pixel offset for a high-resolution camera is limited by the frequency [19]. The higher the observation frequency is, the lower the amplitude of the pixel offset that can be tolerated becomes. Several satellite images are blurred under the influence of micro-vibrations [20]. Thus, the rigid–flexible coupling cannot be ignored and it should be considered in the model of the SOSS.

To fully consider the impact of the resonance on the SOSS system, this study develops a coupling model integrating mechanical, electrical, and control models. We also investigate the impact of rigid–flexible coupling on this model by establishing a rigid–flexible model (R-F-model) and a rigid model (R-model). This study can provide a reference for the design and optimization of the SOSS system.

The following sections of the paper detail our research on the mechanical–electrical–control coupling model. In Section 2, we explain how we derived the transfer function model using the Laplace transform. In Section 3, we present simulations of the R-model and R-F-model acceleration responses under angle tracking mode. We also simulate acceleration responses under different control frequencies to determine the optimal control frequency. Section 4 outlines the experiments we performed and discusses the results. Finally, in Section 5, we summarize our findings and conclude this study.

2. Mechanical–Electrical–Control Coupling Model of the Spaceborne Solar Observation System (SSOS)

The SSOS is an exciting system that comprises a 2D turntable and an observation payload. The 2D turntable contributes majorly to the dynamic response, and it is composed of various components: a motor, a measurement feedback device, a drive controller, and a power supply. Figure 1 depicts the schematic diagram of the system, illustrating that the SSOS is a typical mechanical–electrical–control coupled system.

This section establishes the mechanical–electrical–control coupling model, which consists of mechanical, electrical, and control models. We established the R-F-model and R-model to investigate the influence of the structural flexibility on the model's accuracy.

2.1. Mechanical Model

Based on Newton's Law, the SSOS mechanical dynamics model based on its rotational degrees of freedom is expressed as follows [21]:

$$J_0 \frac{d^2\theta}{dt^2} + B \frac{d\theta}{dt} = T_e - T_l, \quad (1)$$

where θ is the rotation angle, J_0 is the moment of inertia of the motor rotor, B is the damping torque coefficient, T_e is the motor torque, and T_l is the inertial torque. Due to the approximately unconstrained rotation of the rotor, the stiffness part is ignored.

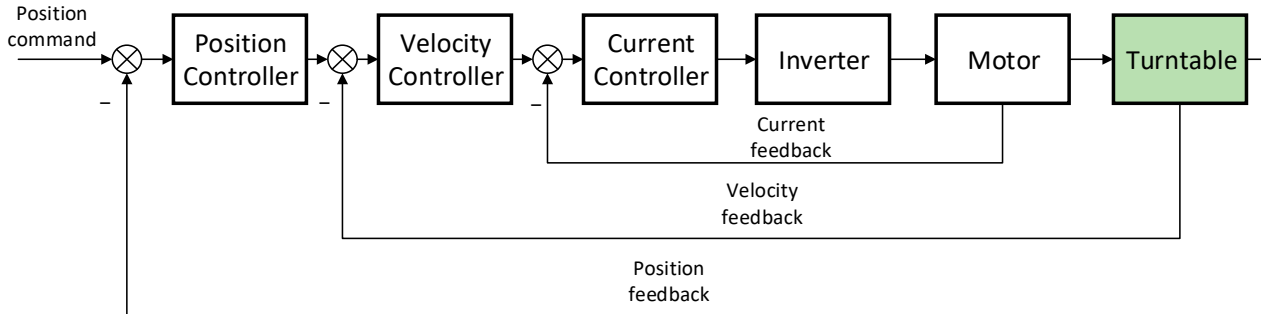


Figure 1. Schematic diagram of the spaceborne solar observation system (SSOS). (⊗ is a summation block and “−” is a minus sign).

The inertial motion of the moving components generates an inertial torque. Therefore, when the structure is assumed to be a rigid body, the angular acceleration of the rotating component generates an inertial torque. The turntable’s motion includes its rigid body motion and elastic vibrations when the structure is assumed to be an elastic body. Therefore, the rigid–flexible coupling characteristics should be considered. The inertial torques of the R-model and R-F-model are established to analyze the impact of the structural flexibility, as follows.

(a) Inertial torque of R-model

Assumptions:

For the R-model, the rotating component is assumed to be a rigid body.

The inertial torque of the rigid body can be expressed as:

$$T_l = J_1 \frac{d^2\theta}{dt^2}, \quad (2)$$

where J_1 is the moment of inertia of the SSOS rotating component.

(b) Inertial torque of R-F-model

Assumptions:

For the R-F-model, the rotating component is assumed to be a flexible body, so the flexible vibration and the rotational motion of the rotating component are coupled.

The rigid–flexible coupled dynamics equations are expressed as follows:

$$\begin{bmatrix} J_1 & \mathbf{m}_p \\ \mathbf{m}_p^T & \mathbf{I}_n \end{bmatrix} \begin{bmatrix} \frac{d^2\theta}{dt^2} \\ \frac{d^2\boldsymbol{\eta}}{dt^2} \end{bmatrix} = \begin{bmatrix} T_l \\ -2\zeta\boldsymbol{\Lambda} \frac{d\boldsymbol{\eta}}{dt} - \boldsymbol{\Lambda}^2\boldsymbol{\eta} \end{bmatrix}, \quad (3)$$

where $\boldsymbol{\eta}$ is the modal coordinate vector, \mathbf{m}_p is the modal participation factor matrix, $\boldsymbol{\Lambda}$ is the modal frequency matrix, \mathbf{I}_n is the n -order identity matrix, n is the modal order, and ζ is the modal damping ratio. Finite element analysis can be used to determine the modal participation factors and modal frequencies, and engineering experience suggests that the modal damping ratio is between 0.03 and 0.05 [22]. The inertial torque can be obtained by solving Equation (3).

2.2. Electrical Model

This section presents the motor torque, and the voltage equation of the motor circuit is expressed as follows:

$$Ri_q + L_q \frac{di_q}{dt} = u_q - u_c, \quad (4)$$

where R is the circuit resistance, i_q is the current, L_q is the inductor, and u_q is the voltage. Moreover, $u_c = K_e d\theta/dt$ is the counter electromotive force generated by the rotation of the motor, and K_e is the counter electromotive force coefficient. The motor torque is expressed as follows:

$$T_e = K_t i_q, \quad (5)$$

where K_t is the motor torque coefficient. The motor voltage and torque equation derivations are presented in Appendix A [23].

2.3. Servo Control Model

The SSOS adopts a three-loop control system, as shown in Figure 1. The speed loop and the current loop are proportional–integral (PI) controllers, with proportional control of the position loop. The control instruction of the position loop is expressed as follows:

$$\omega_r = K_{p\theta} e_\theta, \quad (6)$$

where $e_\theta = \theta_0 - \theta$ is the angle error, θ_0 is the angle instruction, θ is the feedback angle, and $K_{p\theta}$ is the parameter of the position loop controller.

The speed loop control instruction is expressed as follows:

$$i_r = K_{p\omega} e_\omega + K_{i\omega} \int_0^{\Delta t} e_\omega dt, \quad (7)$$

where $e_\omega = \omega_r - \beta\omega$ is the angular velocity error, β is the angular velocity feedback coefficient, ω is the mechanical angular velocity of the motor, $\omega = d\theta/dt$, and $K_{p\omega}$ and $K_{i\omega}$ are the parameters of the speed loop controller.

The control instruction of the current loop is expressed as follows:

$$u_r = K_{pi} e_i + K_{ii} \int_0^{\Delta t} e_i dt, \quad (8)$$

where $e_i = i_r - \alpha i_q$ is the current instruction, α is the current feedback coefficient, and K_{pi} and K_{ii} are the parameters of the current loop controller.

The inverter is simplified as an inertial system, and the relationship between the output voltage and the input voltage is as follows:

$$\frac{du_q}{dt} + \frac{1}{T_{PWM}} u_q = \frac{K_{PWM}}{T_{PWM}} u_r, \quad (9)$$

where K_{PWM} and T_{PWM} are the inverter gain and the time constant, respectively.

2.4. State-Space Equation of the System

This section establishes the state-space equation of the system based on the discussions in Sections 2.1–2.3. The mechanical–electrical–control coupling model is obtained based on Equations (1)–(9):

$$\begin{aligned} L_q \frac{di_q}{dt} + (K_{pi} K_{p\omega} \beta + K_e) \frac{d\theta}{dt} &= G - (R + \alpha) i_q, \\ J_0 \frac{d^2\theta}{dt^2} + B \frac{d\theta}{dt} &= K_t i_q - T_l \end{aligned}, \quad (10)$$

where

$$G = K_{pi} K_{p\omega} K_{p\theta} e_\theta + K_{pi} K_{i\omega} \int_0^{\Delta t} e_\omega dt + K_{ii} \int_0^{\Delta t} e_i dt. \quad (11)$$

The state-space Equation (10) is expressed as follows:

$$\begin{bmatrix} L_q & & & \\ & 1 & & \\ & & J_0 & \\ & & & 1 \end{bmatrix} \frac{d\mathbf{x}}{dt} = \begin{bmatrix} -(R + \alpha) & 0 & -(K_{pi} K_{p\omega} \beta + K_e) & \\ 0 & 0 & 1 & \\ K_t & 0 & -B & \end{bmatrix} \mathbf{x} + \begin{bmatrix} G \\ 0 \\ -T_l \end{bmatrix}. \quad (12)$$

(a) State-space equation of the R-model

We define $i_q = x_1, \theta = x_2, d\theta/dt = x_3$ and combine Equations (2) and (12). The state-space equation of the R-model can be expressed as follows:

$$\begin{bmatrix} L_q & & & & \\ & 1 & & & \\ & & J_0 + J_1 & & \end{bmatrix} \frac{d\mathbf{x}}{dt} = \begin{bmatrix} -(R + \alpha) & 0 & -(K_{pi}K_{p\omega}\beta + K_e) \\ 0 & 0 & 1 \\ K_t & 0 & -B \end{bmatrix} \mathbf{x} + \begin{bmatrix} G \\ 0 \\ 0 \end{bmatrix}. \quad (13)$$

(b) State-space equation of the R-F-model

We define $i_q = x_1, \theta = x_2, \frac{d\theta}{dt} = x_3, d\boldsymbol{\eta}/dt = [x_4, x_5, \dots, x_{n+3}]^T$, and $\boldsymbol{\eta} = [x_{n+4}, x_{n+5}, \dots, x_{2n+3}]^T$, and combine Equations (3) and (12). Then, the state-space equation of the R-F-model can be expressed as follows:

$$\begin{bmatrix} L_q & & & & & & & & \\ & 1 & & & & & & & \\ & & J_0 + J_1 & m_p & & & & & \\ & & m_p^T & I_n & & & & & \\ & & & & I_n & & & & \end{bmatrix} \frac{d\mathbf{x}}{dt} = \begin{bmatrix} -(R + \alpha) & 0 & -K_{pi}K_{p\omega}\beta - K_e & 0 & 0 \\ 0 & 0 & 1 & 0 & 0 \\ K_t & 0 & -B & 0 & 0 \\ 0 & 0 & 0 & -2\zeta\Lambda & -\Lambda^2 \\ 0 & 0 & 0 & I_n & 0 \end{bmatrix} \mathbf{x} + \begin{bmatrix} G \\ 0 \\ 0 \\ 0 \\ 0 \end{bmatrix}. \quad (14)$$

Equation (13) lacks some critical parameters, such as the modal frequency, damping, and participation factor, which are essential in actual structures. In contrast, these parameters significantly contribute to the description of the rigid–flexible coupling characteristics in the state-space equation of the model, as shown in Equation (14). Based on the above information, the importance of the R-F-model is indicated by comparing Equations (13) and (14).

2.5. Transfer Function and Simulink Model of SSOS

It is challenging to quickly determine the impact of the relevant factors on the SSOS performance using the state-space model obtained in Section 2.4. Therefore, we established a Simulink model to simplify the process, which required the use of transfer functions obtained by performing the Laplace transform of each module in Sections 2.1–2.3. The mechanical model's transfer function is expressed as follows:

$$\frac{\theta(s)}{T_e(s) - T_l(s)} = \frac{1}{J_0 s^2 + B s}. \quad (15)$$

The motor transfer function is expressed as follows:

$$\frac{i_q(s)}{u_q(s)} = \frac{1}{R + L_q s} - K_e s \theta(s). \quad (16)$$

The position controller transfer function is expressed as follows:

$$\frac{\omega_r(s)}{e_\theta(s)} = K_{p\theta}. \quad (17)$$

The speed controller transfer function is expressed as follows:

$$\frac{i_r(s)}{e_\omega(s)} = K_{p\omega} + \frac{K_{i\omega}}{s}. \quad (18)$$

The current controller transfer function is expressed as follows:

$$\frac{u_r(s)}{e_i(s)} = K_{pi} + \frac{K_{ii}}{s}. \quad (19)$$

The transfer function of the inverter is expressed as follows:

$$\frac{u_q(s)}{u_r(s)} = \frac{K_{PWM}}{1 + T_{PWM}s}. \tag{20}$$

The transfer function of the inertial torque of the R-model is expressed as follows:

$$\frac{T_l(s)}{\theta(s)} = J_1 s^2. \tag{21}$$

The transfer function of the inertial torque of the model is expressed as follows:

$$\frac{T_l(s)}{\theta(s)} = J_1 s^2 - m_p \left(I_n s^2 + \Lambda^2 + 2\xi \Lambda s \right)^{-1} m_p^T s^4. \tag{22}$$

Note that $T_l(s) = T_{l0}(s) + T_f(s)$, where $T_{l0}(s)$ is the rigid torque, and $T_f(s)$ is the flexible torque. Then, Equation (22) is divided into two parts, where the transfer function of the rigid torque is expressed as follows:

$$\frac{T_{l0}(s)}{\theta(s)} = J_1 s^2. \tag{23}$$

The transfer function of the flexible torque is expressed as follows:

$$\frac{T_f(s)}{\theta(s)} = m_p \left(I_n s^2 + \Lambda^2 + 2\xi \Lambda s \right)^{-1} m_p^T s^4. \tag{24}$$

As illustrated in Figure 2, we combined the transfer functions of the modules mentioned above to create two schematic diagrams, where (a) shows the schematic diagram of the R-model, and (b) shows the schematic diagram of the R-F-model.

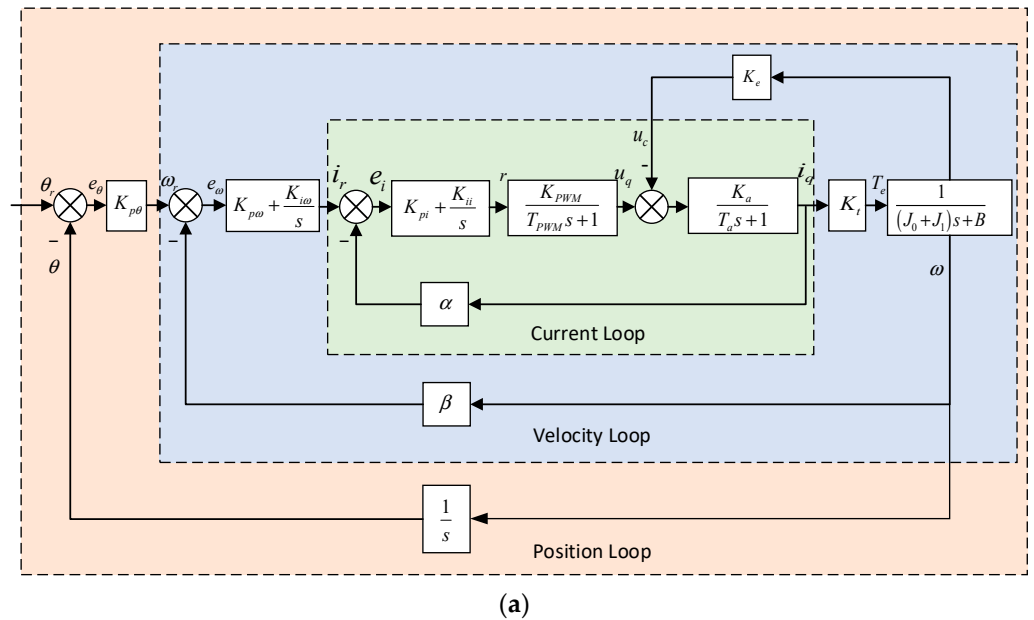


Figure 2. Cont.

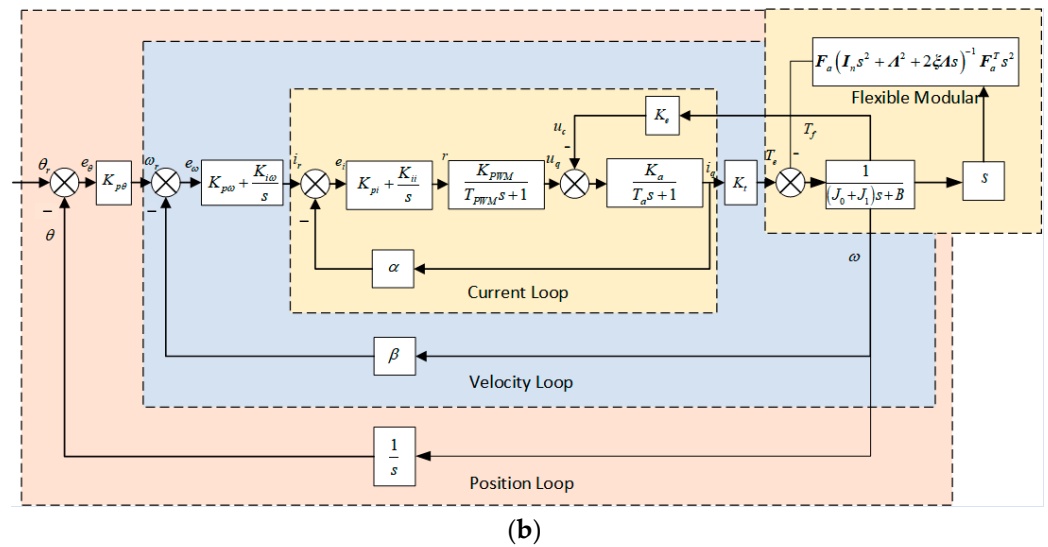


Figure 2. Schematic diagrams of transfer functions of the system (\otimes is a summation block and “−” is a minus sign): (a) schematic diagram of the rigid model (R-model), and (b) schematic diagram of the rigid-flexible model (R-F-model).

3. Simulations of SSOS

We established a Simulink model to analyze the SSOS dynamic characteristics based on the schematic diagram in Section 2. The natural frequency of the turntable may couple with the excitation frequency, causing resonance. Therefore, it is necessary to calculate the natural frequency of the turntable structure. These external excitations may arise from the control frequency of the motor, motor noise, and nonlinear factors. Thus, we built a finite element method (FEM) model of the 2D turntable to investigate the effect of the rigid-flexible coupling characteristics. Moreover, we obtained the modal frequencies and participation factors [8,9] of the SSOS through FEM analysis and additional calculations.

3.1. Finite Element Method (FEM) Modeling and Simulations of Two-Dimensional (2D) Turntable

3.1.1. FEM Model and Modal Analysis

The 2D turntable has dimensions of 463 mm × 336 mm × 550 mm and weighs 23 kg. The 2D turntable FEM model was established. A mesh convergence study was conducted and mesh size 10 was adopted. The first 10 modes were calculated through modal analysis. Figure 3 depicts the first three modal deformation cloud diagrams, and Table 1 presents the first 10 modal frequencies. The natural frequencies of the 2D turntable are all higher than 100 Hz, and 0.03 is the modal damping ratio.

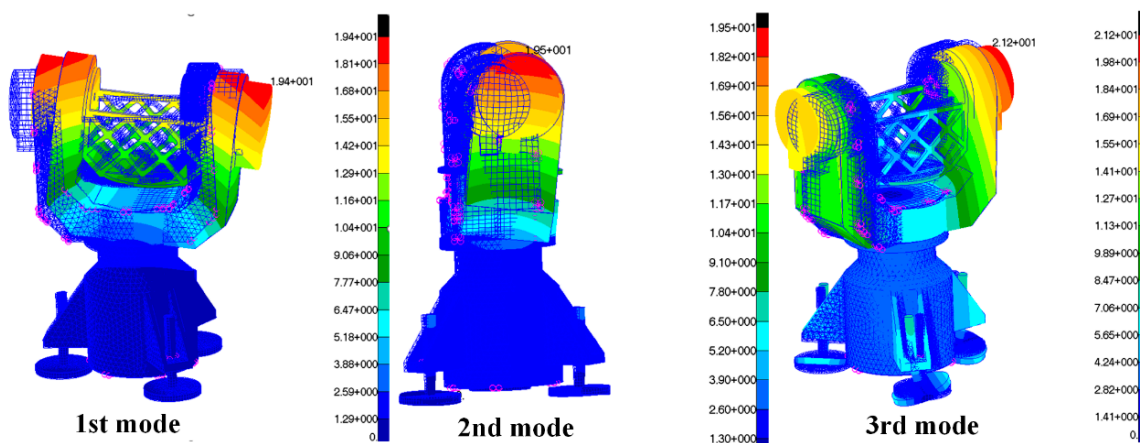


Figure 3. First three modal deformation cloud diagrams.

Table 1. Modal frequency and participation factors.

	1	2	3	4	5	6	7	8	9	10
Modal frequency	119.6	133.0	180.2	314.1	332.6	465.0	472.1	635.3	647.9	667.2
X	−0.026	−1.116	−0.111	0.004	−0.280	0.012	−0.020	−0.003	−0.003	5×10^{-5}
Y	−0.006	0.056	−0.390	-1×10^{-5}	−0.005	0.063	−0.088	−0.005	−0.006	0.001
Z	−1.124	0.024	0.016	0.389	0.003	0.002	−0.001	−0.002	−0.004	0.016

3.1.2. Modal Participation Factors

Since the turntable only moves via rotation, the rotational modal participation factor is expressed as follows:

$$\mathbf{m}_p = \sum_{i=1}^N m_i \mathbf{r}_i \times \boldsymbol{\Phi}_i, \quad (25)$$

where m_i represents the mass of node i , N is the total number of nodes, $\mathbf{r}_i \in R_{1 \times 3}$ is the vector of node i relative to the reference point, and $\boldsymbol{\Phi}_i \in C_{3 \times n}$ represents the modal vector matrix of node i , where n is the modal truncation order. We calculated the generalized modal effective mass and its proportional factor relative to the moment of inertia to determine the modal truncation order. The modal effective mass of the first n modes is expressed as follows:

$$\mathbf{M}_{eff}(n) = \mathbf{m}_p(n) \mathbf{m}_p^T(n). \quad (26)$$

The proportional factor of the first n modal effective masses is expressed as follows:

$$factor(n) = \frac{1}{3} \left(\frac{\mathbf{M}_{eff11}(n)}{J_{xx}} + \frac{\mathbf{M}_{eff22}(n)}{J_{yy}} + \frac{\mathbf{M}_{eff33}(n)}{J_{zz}} \right). \quad (27)$$

We computed the first 10 modes' participation factors (unit: $m \cdot \sqrt{\text{kg}}$) based on Equation (25), and the results are presented in Table 1. Moreover, we calculated the first five modes' proportional factors, based on Equations (26) and (27), as shown in Figure 4, where each column represents the proportional factor of the first n modes. The larger the proportional factor is, the closer it is to the actual vibration.

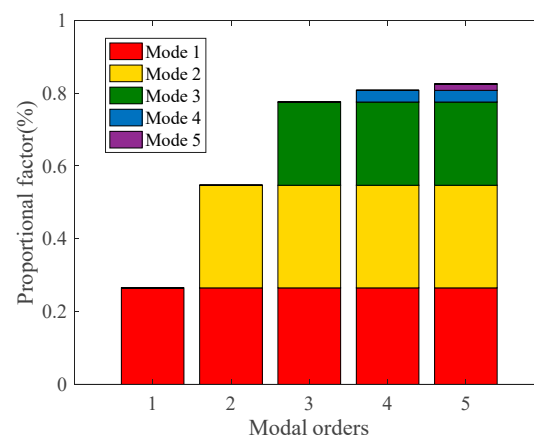
**Figure 4.** Proportional factors of the first five modal effective masses.

Figure 4 shows that the modal proportional factors of the first three modes reached 80%. As the modal order increased, the proportional factor increased slightly. As a result, the modal truncation order was selected as 3 in the simulation, considering both the accuracy and the calculation complexity.

3.2. Simulation of SSOS

In this section, we established a Simulink model, which was used to perform simulations with the R-model and R-F-model to analyze the impact of rigid–flexible coupling on the turntable’s rotation angles and acceleration responses. Thereafter, we performed simulations with the R-model and R-F-model for different control frequencies to obtain the optimal value of the control frequency. The control frequency represents the number of instruction signals per second. In order to avoid resonance caused by coupling between the control frequency and the natural frequency of the turntable, we selected control frequencies that are lower than 1/10 of the turntable’s natural frequency.

3.2.1. Simulink Model

The Simulink simulation model of the R-F-model was built based on the schematic diagram in Figure 2. Some parameters of the turntable’s pitch axis are presented in Table 2, and the flexible module was disabled when R-model simulations were conducted.

Table 2. System parameters.

Parameter	Value	Parameter	Value
$K_{p\theta}$	38.18	K_e	0.19
$K_{p\omega}$	18.84	K_t	0.21
$K_{i\omega}$	6.27	L_q	9.6×10^{-4} (H)
K_{pi}	2.02	R	1.56 (Ω)
K_{ii}	315.13	T_a	6.17×10^{-4}
K_{PWM}	13.86	K_a	0.64
T_{PWM}	0.001	J_1	0.036 ($\text{kg}\cdot\text{m}^2$)
B	0.0033	J_0	7.21×10^{-5} ($\text{kg}\cdot\text{m}^2$)

3.2.2. Acceleration Response Simulation under Angle Tracking Mode

The SSOS mainly operates in an angle tracking mode, and its axis always points to the Sun. The solar altitude from 6:00 to 6:01 on March 24 was selected based on the simulation input data, and the control frequency was 1 Hz. Figure 5a shows the tracking angle of the R-F-model and R-model, where the red solid line is the curve of the R-F-model. The green dotted line is the curve of the R-model, and the blue dashed line is the input angle. Figure 5b depicts the R-F-model and R-model angle tracking errors. Figure 5 shows that the angles of the R-F-model and R-model are similar, and the angle tracking errors are less than 5". Based on this figure, theoretically, the turntable’s structural flexibility with high natural frequencies has little influence on the angle tracking.

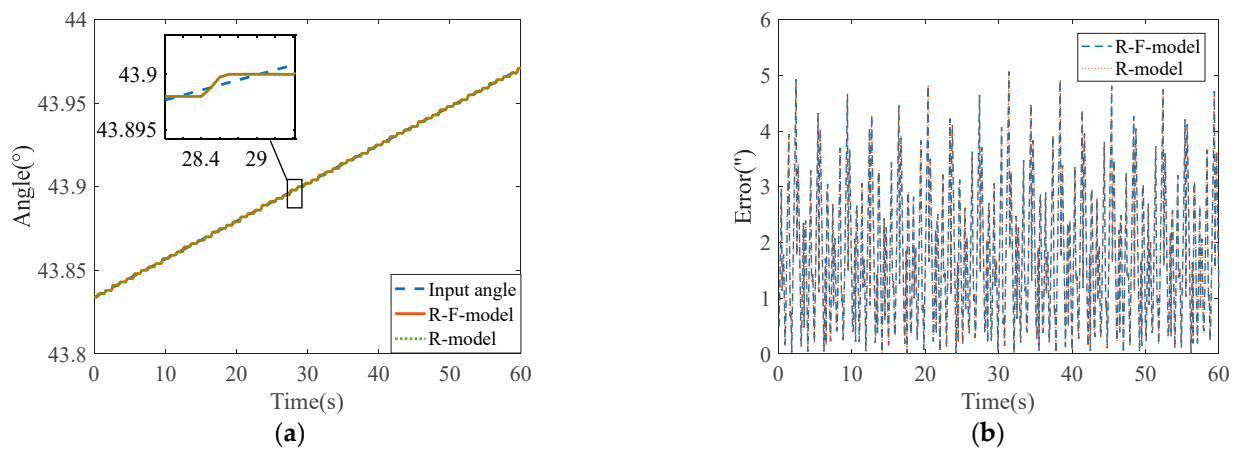


Figure 5. Solar altitude angle: (a) tracking angles of the two models and (b) tracking errors of the two models.

Figure 6 shows the acceleration spectral curves, indicating that the acceleration spectra of the R-F-model generated peak responses in high frequencies caused by structural flexibility compared with the R-model. Eventually, the extra responses caused by the structural flexibility would affect the SSOS. The simulation results indicate that the rigid–flexible coupling characteristic has little influence on the angle tracking of the simulation model. However, this rigid–flexible coupling affects the high-frequency distribution of the acceleration spectrum. This mechanism is essential for a spaceborne SSOS, as micro-vibrations at a high frequency may negatively affect the satellites’ stable precision and the image definition of optical cameras. Therefore, this issue requires attention, which is verified in Section 4. Overall, the proposed coupling model can describe the difference between the R-model and the R-F-model.

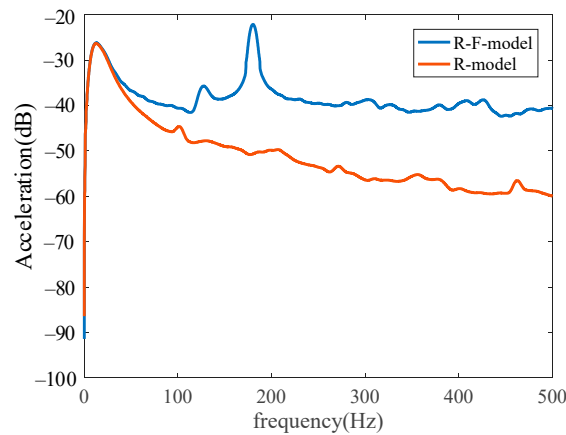


Figure 6. Acceleration spectra.

3.2.3. Acceleration Response Simulations under Various Control Frequencies

We input the angle commands at different frequencies to conduct dynamic simulations, selecting the solar altitude from 6:00 to 6:01 on March 24 as the simulation input data, where the control frequencies were 0.2, 1, 2, 5, and 10 Hz. The maximum angle tracking error curves under different control frequencies were obtained through simulations, as shown in Figure 7, where the solid blue line is the R-F-model’s simulation result, and the dashed red line is the R-model’s simulation result. These results indicate that the angle tracking error decreases as the control frequency increases. The maximum angle tracking error is less than 5", and it satisfies the angle tracking requirement when the control frequency is higher than 1 Hz.

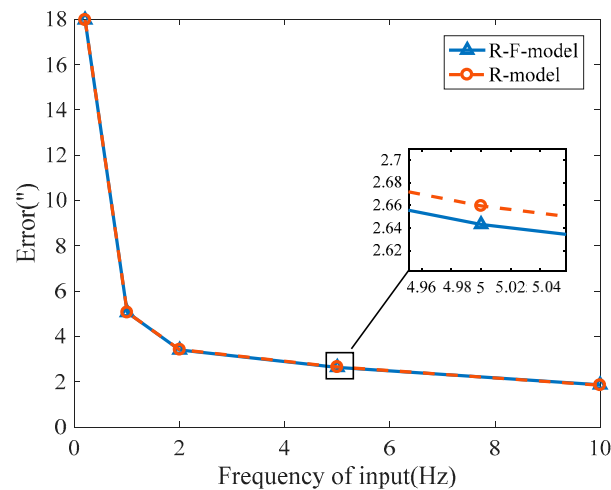


Figure 7. Maximum angle tracking errors under different control frequencies.

Figure 8 shows the acceleration spectral curves under different control frequencies, where (a) shows the acceleration spectral curve of the R-F-model, and (b) shows the acceleration spectral curve of the R-model. The third modal frequency of the turntable is 180.2 Hz (Table 1), which amplifies the vibration of the turntable, resulting in a peak acceleration at about 180 Hz in Figure 8. Moreover, the acceleration peak value increases as the control frequency increases. We calculated the acceleration response's root mean square (RMS) values under different control frequencies, as shown in Figure 9a. Interestingly, the RMS of the acceleration response of the R-F-model is two times larger than that of the R-model. The RMS of the acceleration response shows an upward trend as the control frequency increases. To obtain the optimal control frequency of the SSOS, the acceleration RMS and maximum angle tracking error were plotted, as shown in Figure 9b. The acceleration RMS and the angle tracking error shows opposite trends. When the input frequency was 2 Hz, the angle tracking error is less than $5''$, lower than the precision SSOS requirement. The angle tracking error tends to be convergent, and the acceleration RMS is relatively small at the same time. As a result, 2 Hz was selected as the control frequency when developing the SSOS.

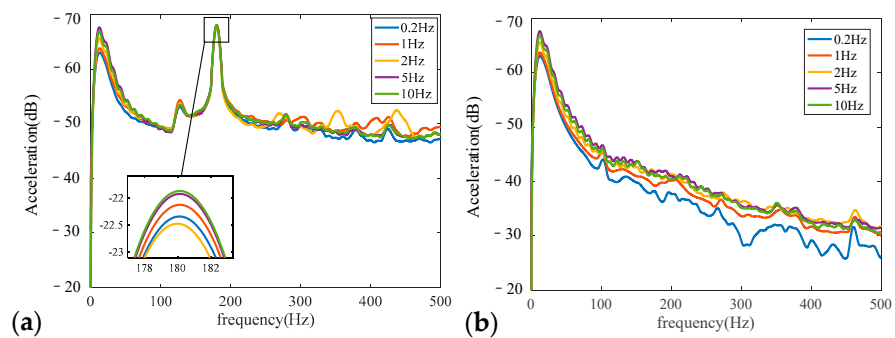


Figure 8. Acceleration spectral curves: (a) acceleration spectra of the R-F-model and (b) acceleration spectra of the R-model.

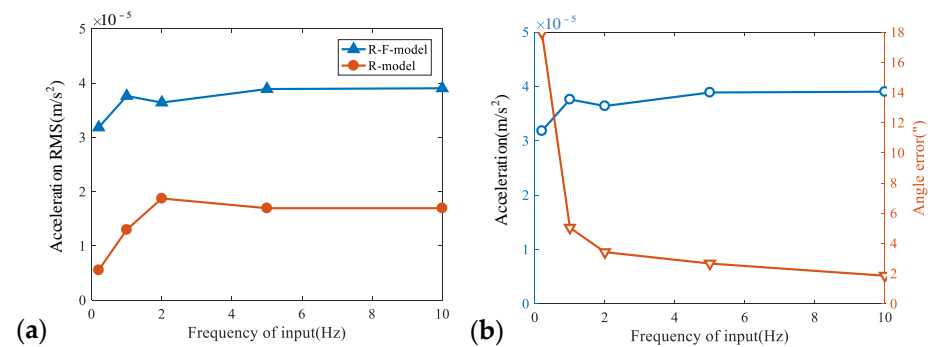


Figure 9. (a). Acceleration root mean square (RMS) under different control frequencies. (b) Acceleration RMS and maximum angle tracking error of R-F-model (the blue circles represent the acceleration RMS, and the red triangles represent the angle tracking error).

4. Experiments

We set up an SSOS experimental system to further prove the effectiveness of the coupling model and the research value of flexible features in high-accuracy spaceborne tracking instruments.

4.1. Experiment Setup

Figure 10a shows that the experimental system comprised a 2D turntable, three accelerometers, a signal acquisition system, a controller, a power supply, and a computer with control software. The type of the controller is Elmo's BMTWID20SE. The accelerometers (P1,

P2, and P3) were mounted on the rotating component of the 2D turntable. The experimental setup is shown in Figure 10b. The angle command curve was input to the control software to realize a continuous observation of the Sun, and the control frequencies were set to 1, 2, 5, and 10 Hz.

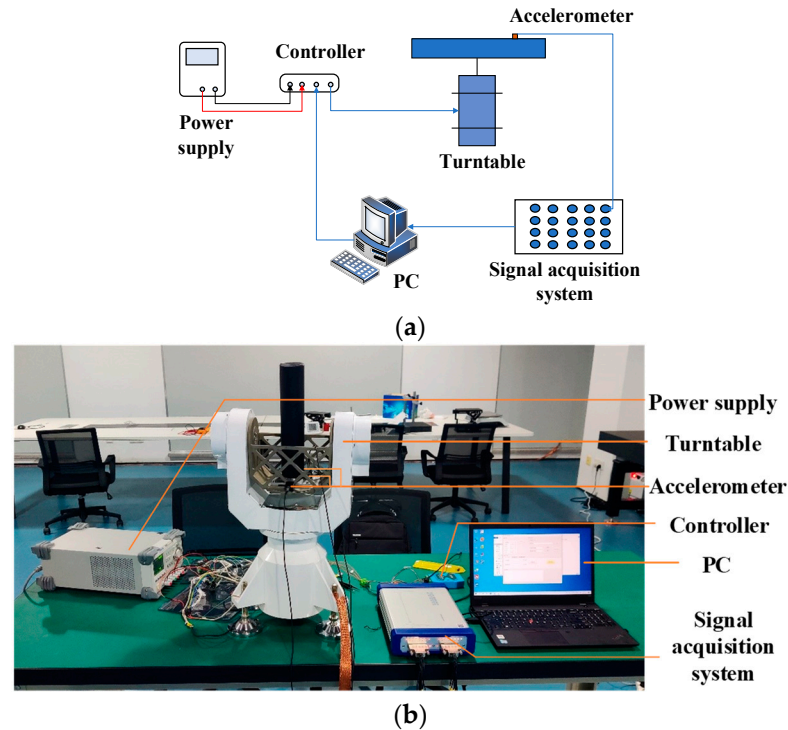


Figure 10. Experimental system: (a) schematic diagram and (b) experimental site.

4.2. Processing and Analysis of Experimental Data

Figure 11 shows the acceleration spectral curves, which are measured using accelerometers. The control frequency is 2 Hz, where the blue solid, red dashed, and yellow dotted-dashed curves represent the acceleration results measured using P1, P2, and P3, respectively. The purple dotted curve shows the R-F-model simulation result, while the green curve shows the R-model simulation result. The measured acceleration results show that there are peaks between 100 and 200 Hz, indicating that resonances are generated by the coupling of the turntable's structural modes and the excitation frequency. The R-F-model simulation result replicates the 2D turntable's vibration characteristics in the high-frequency regions, and its predictions were closer to the experimental results than those of the R-model. The results showed that the mechanical–electrical–control coupling model could better reflect the SSOS dynamic characteristics than the traditional rigid-body model when considering rigid–flexible coupling characteristics.

We conducted tests to measure the acceleration responses at different control frequencies (1, 2, 5, and 10 Hz). In Table 3, the experimental results of the acceleration peak values and the corresponding frequencies are compared with those obtained with the R-F-model. The average error of the frequencies is approximately 10.3%, while the average error of the peak value is approximately 29.9%. The frequency errors of the R-F-model are smaller than the ones of the R-model. However, the peak value errors are relatively large because it is difficult to simulate all system characteristics, such as the structural damping ratio and the nonlinear factors. However, the simulation model still simulates the high-frequency vibrations of the system. The simulation results can help to predict the micro-vibration frequencies and provide suggestions for vibration isolation design.

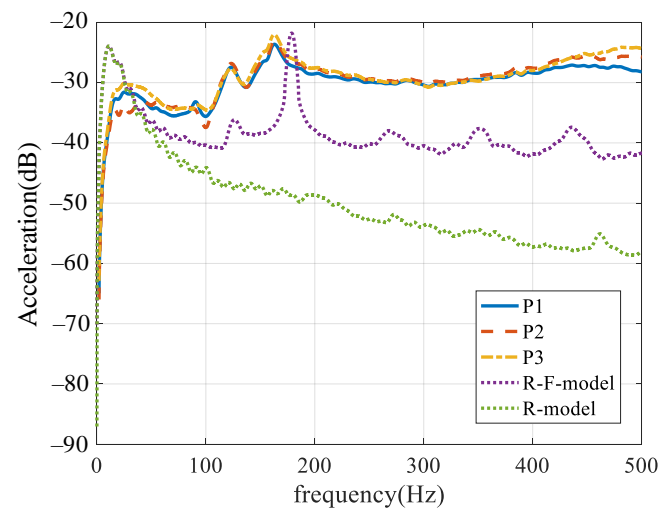


Figure 11. Comparison of experimental and simulation results of acceleration.

Table 3. Frequencies and peak values of the simulations and experiments.

	Frequency of Simulation (Hz)	Frequency of Experiment (Hz)	Frequency Error	Peak Value of Simulation (m/s^2)	Peak Value of Experiment (m/s^2)	Peak Value Error
1 Hz	177.5	161.3	10.0%	0.0077	0.0055	44.0%
2 Hz	177.1	160.8	10.1%	0.0081	0.0063	28.6%
5 Hz	177.3	160.8	10.3%	0.0092	0.0073	26.0%
10 Hz	177.6	160.5	10.7%	0.0093	0.0077	20.8%

5. Conclusions

The purpose of this study is to investigate how the elastic characteristics and control frequency impact micro-vibration acceleration responses in a high-precision SSOS. To achieve this goal, we developed the R-F-model and R-model of the SSOS, and analyzed the effect of rigid–flexible coupling by establishing the state-space model. We then built a Simulink model using the Laplace transform to derive a transfer function model. By simulating the R-F and R-model acceleration responses under the angle tracking mode, we observed differences when flexible features were considered. Specifically, the RMS of the model’s acceleration response was found to be two times larger than that of the R-model. We also conducted simulations with various control frequencies to determine the optimal value. Finally, we conducted experiments and validated the theoretical model and simulation results using measured data under different control frequencies (1, 2, 5, and 10 Hz). Our findings suggest that the flexibility of the structure affects the high-frequency distribution of the acceleration spectra and poses threats to the high tracking accuracy. This study highlights the significance of elastic structures in dynamic response and provides a valuable reference for the design and micro-vibrations of spacecraft structure systems.

Author Contributions: Conceptualization, L.Y.; methodology, Y.W.; software, Y.W.; validation, L.W.; investigation, Y.C.; writing—original draft preparation, Yan-song Wang and Lin Yang.; writing—review and editing, L.W. and Y.C.; visualization, Y.W.; supervision, Y.C.; funding acquisition, L.Y. All authors have read and agreed to the published version of the manuscript.

Funding: This work was supported by the National Natural Science Foundation of China (No. 12203032) and the Natural Science Foundation of Shandong Province (ZR2022QA030).

Data Availability Statement: The data presented in this study are available on request from the corresponding author.

Conflicts of Interest: The authors declare no conflicts of interest.

Appendix A

In the d - and q -axis coordinate systems [23], the motor magnetic linkage equations are expressed as follows:

$$\begin{aligned}\Psi_d &= L_d i_d + \Psi_m \\ \Psi_q &= L_q i_q\end{aligned}, \quad (A1)$$

where Ψ_d and Ψ_q are the magnetic linkages along the d -axis and q -axis, respectively; L_d and L_q are the inductances along the d -axis and q -axis, respectively; i_d and i_q are the currents along the d -axis and q -axis, respectively; and Ψ_m is the magnetic linkage of the permanent magnet.

The voltage equations of the motor are expressed as follows:

$$\begin{aligned}u_d &= R i_d + \frac{d\Psi_d}{dt} - \omega_e \Psi_q = R i_d + L_d \frac{di_d}{dt} + \frac{d\Psi_m}{dt} - \omega_e \Psi_q \\ u_q &= R i_q + \frac{d\Psi_q}{dt} + \omega_e \Psi_d = R i_q + L_q \frac{di_q}{dt} + \omega_e \Psi_d\end{aligned}, \quad (A2)$$

where u_d is the voltage along the d -axis, u_q is the voltage along the q -axis, ω_e is the electrical angle, $\omega_e = p_n \frac{d\theta}{dt}$, p_n represents the pole pairs of the motor, θ is the motor angle, and R is the resistance.

The motor torque equation is expressed as follows:

$$T_e = p_n [\Psi_m i_q + (L_d - L_q) i_d i_q], \quad (A3)$$

where the first term is the magnetic excitation force, and the second term is the magnet restraining torque.

Using the $i_d = 0$ control strategy, the required current is the minimum, and the maximum torque can be obtained per unit current. In this case, the magnetic linkage is expressed as

$$\begin{aligned}\Psi_d &= \Psi_m \\ \Psi_q &= L_q i_q\end{aligned}. \quad (A4)$$

and the voltage equations are expressed as

$$\begin{aligned}u_d &= \frac{d\Psi_m}{dt} - \omega_e L_q i_q \\ u_q &= R i_q + L_q \frac{di_q}{dt} + \omega_e \Psi_m\end{aligned} \quad (A5)$$

References

- Li, C.; Chen, Y.; Ni, S.; Tan, B.; Zhang, Z. PIC Simulation of Double Plasma Resonance and Zebra Pattern of Solar Radio Bursts. *Astrophys. J. Lett.* **2021**, *909*, L5. [CrossRef]
- Ni, S.; Chen, Y.; Li, C.; Zhang, Z.; Hosseinpour, M. Plasma Emission Induced by Electron Cyclotron Maser Instability in Solar Plasmas with a Large Ratio of Plasma Frequency to Gyrofrequency. *Astrophys. J. Lett.* **2020**, *891*, L25. [CrossRef]
- Anashin, V.; Chubunov, P.; Koziukov, A.; Konyukhov, A.; Protopopov, G. Challenges and Approaches to Radiation Hardness Control of Electronic Components to In-Space High-Energy Particles Exposure. In Proceedings of the 2018 20th International Symposium on High-Current Electronics (ISHCE), Tomsk, Russia, 16–22 September 2018.
- Nagabhushan, V.; Fitz-Coy, N.G. On-orbit jitter control in momentum actuators using a three-flywheel system. *Acta Astronaut.* **2014**, *95*, 61–81. [CrossRef]
- Yang, L.; Wang, Y.; Wei, L. A novel identification method for micro-vibration analysis of reaction wheel assembly. *Acta Astronaut.* **2022**, *196*, 94–106. [CrossRef]
- Lin, L.; Tan, L.; Lin, K.; Dong, W.; Yang, H. The influence of flywheel micro vibration on space camera and vibration suppression. *Mech. Syst. Signal Process.* **2018**, *100*, 360–370.
- Sattar, M.; Wei, C. Analysis of coupled torsional disturbance behavior of micro-stepped solar array drives. *J. Sound. Vib.* **2019**, *442*, 572–597. [CrossRef]
- Kouritem, S.A.; Elshabasy, M.M.Y.B. Tailoring the panel inertial and elastic forces for the flutter and stability characteristics enhancement using copper patches. *Compos. Struct.* **2021**, *274*, 114311. [CrossRef]
- Bani-Hani, M.A.; Almomani, A.M.; Aljanaideh, K.F.; Kouritem, S.A. Mechanical Modeling and Numerical Investigation of Earthquake-Induced Structural Vibration Self-Powered Sensing Device. *IEEE Sens. J.* **2022**, *22*, 19237–19248. [CrossRef]
- Yang, L.; Wang, Y.; Wei, L.; Chen, Y. Identification of reaction wheel assembly disturbances based on variable modal frequencies. *Mech. Syst. Signal Process.* **2023**, *205*, 110868. [CrossRef]

11. Wang, Z.; Wang, X.; Wang, T.; Zhang, B.; Ma, H. Accuracy Analysis and Motion Control of Two-axis Nonmagnetic Turntable Based on Ultrasonic Motor. *Mechanika* **2020**, *26*, 221–230. [[CrossRef](#)]
12. Sun, G.; Wang, M.; Yao, X.; Wu, L. Fault detection of switched linear systems with its application to turntable systems. *J. Syst. Eng. Electron.* **2011**, *22*, 120–126. [[CrossRef](#)]
13. Liu, Y.G.; Zhang, H.Z.; Hu, H.; Li, Y.L. Design and Finite Element Analysis of Large Target Tracking Turntable. In Proceedings of the Chinese Guidance, Navigation and Control Conference, Nanjing, China, 12–14 August 2016; IEEE: Piscataway, NJ, USA, 2016; pp. 2043–2047.
14. Zhang, Y.; Liu, Z.; Li, Z. Modal analysis of collimation frame for Space two-dimensional turntable. In Proceedings of the 5th International Conference on Material Science and Engineering, Guangzhou, China, 24–26 June 2016.
15. Zou, D.; Li, Z.; Liu, Z.; Cui, K.; Zhang, Y.; Zhou, L. Modal simulation and experimental verification of Space-borne two dimensional turntable. In Proceedings of the Applied Optics and Photonics China (AOPC2017), Beijing, China, 4–6 June 2017; SPIE: Bellingham, WA, USA, 2017.
16. Sun, L.; Ma, H.; Zhao, Z. Optimization Design of Aerial Work Vehicle Turntable Based on Topology Optimization. In Proceedings of the 2nd IYSF Academic Symposium on Artificial Intelligence and Computer Engineering, Xi'an, China, 8–10 October 2021; Qin, W., Ed.; SPIE: Bellingham, WA, USA, 2021.
17. Li, J. Optimization Design of the Precision Optoelectronic Tracking Turntable Frame. In Proceedings of the 5th International Symposium on Advanced Optical Manufacturing and Testing Technologies, Dalian, China, 26–29 April 2010; Luo, X., VanFreyman, G., Eds.; SPIE: Bellingham, WA, USA, 2010.
18. Yao, H.; Huang, Y.; Ma, W.; Liang, L.; Zhao, Y. Dynamic Analysis of a Large Deployable Space Truss Structure Considering Semi-Rigid Joints. *Aerospace* **2023**, *10*, 821. [[CrossRef](#)]
19. Chen, S.B.; Xuan, M.; Xin, J.; Liu, Y.; Gu, S.; Li, J.; Zhang, L. Design and experiment of dual micro-vibration isolation system for optical satellite flywheel. *Int. J. Mech. Sci.* **2020**, *179*, 105592. [[CrossRef](#)]
20. Yang, L.; Wang, Y.S. Study of the multi-excitation decoupling optimization method for the integrated structure of a high-resolution optical satellite. *J. Vib. Control* **2023**, *29*, 2086–2101. [[CrossRef](#)]
21. Taylor, J.E. *Theoretical Mechanics*; Legare Street Press: Charleston, SC, USA, 2022.
22. Heylen, W. *Modal Analysis Theory and Testing*, 2nd ed.; Katholieke Universiteit Leuven, Departement Werktuigkunde Press: Leuven, Belgium, 1998.
23. Zhu, Q.; Xiong, L.; Liu, H. A robust speed controller with smith predictor for a PMSM drive system with time delay. *Int. J. Control Autom. Syst.* **2017**, *15*, 2448–2454. [[CrossRef](#)]

Disclaimer/Publisher's Note: The statements, opinions and data contained in all publications are solely those of the individual author(s) and contributor(s) and not of MDPI and/or the editor(s). MDPI and/or the editor(s) disclaim responsibility for any injury to people or property resulting from any ideas, methods, instructions or products referred to in the content.